Electronic Supporting Information

Quantitative Characterization and Modeling of Multiphase Flow in Structured Microreactors: A Post Microreactor Case Study

Lu Yang[a], Yanxiang Shi[b], Milad Abolhasani[a] and Klavs F. Jensen[a,*]

[a] Dept. Chem. Eng., Massachusetts Institute of Technology, Cambridge, MA 02139, USA

[b] BASF Corporation, Beachwood, OH 44122, USA

S1. Methods

S1.1 Automated image processing

Using the images obtained from the laser-induced fluorescence (LIF) visualization, automated image processing can be performed to analyze the corresponding phase holdup and interfacial areas. All the following image analysis routines on a single image were performed using ImageJ 1.47v (National Institute of Health, USA).[1] To obtain the phase holdup, we first converted the image into the 8-bit format and applied a threshold to distinguish between the fluorescent and non-fluorescent phases. The total area of the white pixels corresponded to the area occupied by the fluorescent phase (1.507 mm^2 in Figure S1). To obtain the total reactor volume in the same field of view, we took a reference picture in which the entire reactor was filled with the fluorescent phase only. After the same processing, the total area of the white pixels in the reference corresponded to the total reactor volume (2.315 mm^2 in Figure S1). The ratio of the two numbers yielded the fluorescent phase holdup. Subtracting the fluorescent phase holdup from unity gave the non-fluorescent phase holdup.

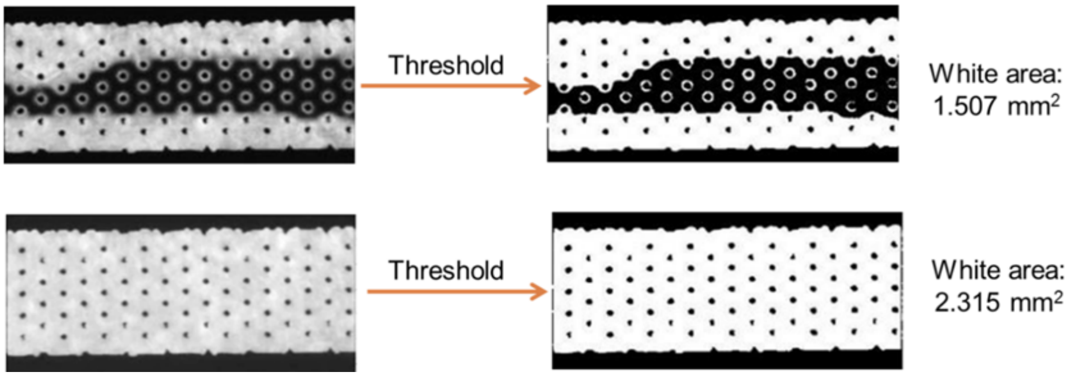

$$\text{Fluorescent Phase Holdup} = \frac{1.507}{2.315} = 0.651$$

$$\text{Non} - \text{fluorescent Phase Holdup} = 1 - 0.651 = 0.349$$

Figure S1. Representative quantification of phase holdup using image analysis

To obtain the specific interfacial area, we first applied the "find edge" utility in ImageJ, which traced out all the boundaries between black and white pixels in a binarized picture. In this case, the boundaries included not only the fluid/fluid interface, but also the reactor contour (i.e., the fluid/solid interface). We then performed the same routine to the reference picture, which yielded only the reactor contour. Subtracting the two sets of boundaries produced the fluid/fluid interface only, and its total length could then be calculated. For a two-dimensional image, dividing the total length of the interface by the total internal area of the reactor yields the specific interfacial area.

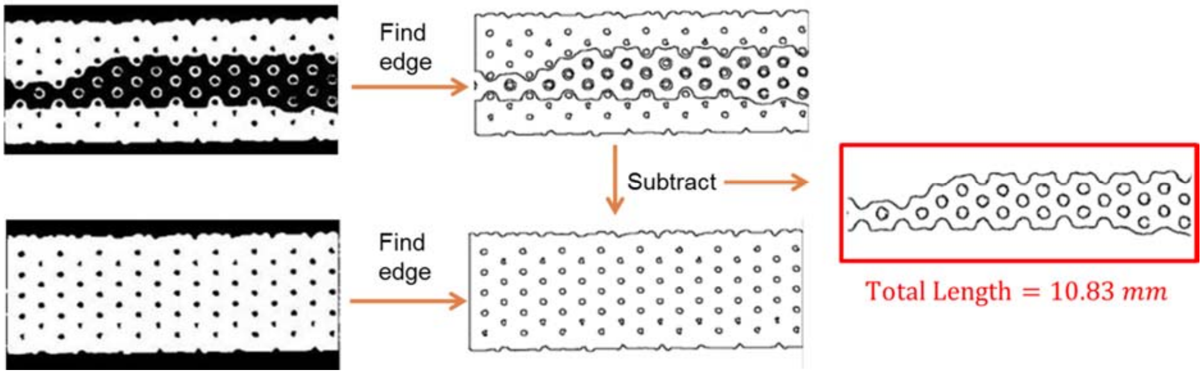

$$\text{Specific Interfacial Area} = \frac{\text{Length of Interface}}{\text{Total Area}} = \frac{10.83\ \text{mm}}{2.315\ \text{mm}^2} = 4.68\ mm^{-1}$$

Figure S2. Quantification of specific interfacial area using image analysis

The above procedure allows us to extract the holdup and interfacial area of a single frame of image. To automatically analyze the sequence of images obtained from experiment and numerical simulations, we employed MIJ (EPFL, Switzerland),[2] a Java package for communication and data exchange between ImageJ and Matlab (R2013a, MathWorks Inc., Natick, MA, USA). This software enabled us to loop through the images with Matlab's control algorithm, analyze each image using ImageJ's functionalities, and store the numeric results using Matlab, thus achieving automated analysis of the image sequences.

S1.2 The volume-of-fluid method

The volume-of-fluid (VOF) method is a Eulerien method that is widely used in simulating multiphase flow on the microscale. In the VOF method,[3] a key variable is the phase volume fraction α_k in a given cell. Assuming the liquid phase fraction to be α_1 in a gas/liquid flow, then for cells within the liquid phase, $\alpha_1 = 1$; and for cells within the gas phase, $\alpha_1 = 0$. The case of $0 < \alpha_1 < 1$ only occurs when the gas/liquid interface exists within the cell. Although in this representation, the interface has a thickness of at least one cell, the accurate tracking of interface becomes possible when a fine enough mesh is used.

Naturally, the continuity equation can be written on the basis of the phase volume fraction α_k for each phase k:

$$\frac{\partial(\rho_k \alpha_k)}{\partial t} + \nabla \cdot (\rho_k \alpha_k \boldsymbol{u_k}) = S_m$$

$$\sum_{k=1}^{k=\text{n}} \alpha_k = 1$$

Because the interface is represented by a discontinuous jump in the volume fraction, the interface has a high tendency to be smeared out through numerical handling of this step function. This problem can be improved to a certain degree by adding an interfacial compression term to the transport equation of α_k, as is executed in the interFoam solver in OpenFOAM. [4]

A distinct feature of the VOF method is the one-fluid formulation that solves a single momentum and continuity equations throughout the entire computation domain:

$$\frac{\partial(\rho_m \boldsymbol{u})}{\partial t} + \boldsymbol{\nabla} \cdot (\rho_m \mathbf{u} \times \mathbf{u}) = \mu_m \nabla^2 \boldsymbol{u} - \boldsymbol{\nabla}\mathrm{P} + \rho_m \boldsymbol{g} + \boldsymbol{F_{st}}$$

$$\boldsymbol{\nabla} \cdot \boldsymbol{u} = \mathbf{0}$$

Here, $\mathbf{F_{st}}$ refers to the surface tension force, which is often converted into a body force based on the continuous surface force model (CSF).[5] For cells containing phase boundaries ($0 < \alpha_1 < 1$), the density and viscosity values are approximated by a linear interpolation of the adjacent phases.

$$\rho_m = \sum_{k=1}^{n} \alpha_k \, \rho_k$$

$$\mu_m = \sum_{k=1}^{n} \alpha_k \, \mu_k$$

By using a single momentum equation, the VOF method circumvents the need to approximate interfacial interactions by constitutive equations, which increases the accuracy of result. Due to its ease of tracking the interface, the VOF method has been widely applied when modeling multiphase flow in microreactors.

S1.3 Numerical model and discretization

Our multiphase flow simulation was performed using the finite-volume method code OpenFOAM.[6] The transient terms in the model equations were discretized using an implicit Euler scheme. The spatial discretization was achieved by a TVD scheme with limited linear differencing. The phase fraction function was discretized using a special scheme provided by OpenFOAM named *interfaceCompression*, which implemented the MULES (Multidimensional Universal Limiter with Explicit Solution) algorithm to ensure the boundedness of the function.

Meshing for the post microreactor interior was performed using a commercial grid generator, Pointwise V17.1R4 (Pointwise, Inc., Fort Worth, TX, USA), with a total of 80,000 hexahedral cells (Figure S3). As shown in Figure S3b, the mesh is able to preserve all the physical features of the post microreactor interior, with extra-fine mesh close to the posts to capture the boundary layer effects.

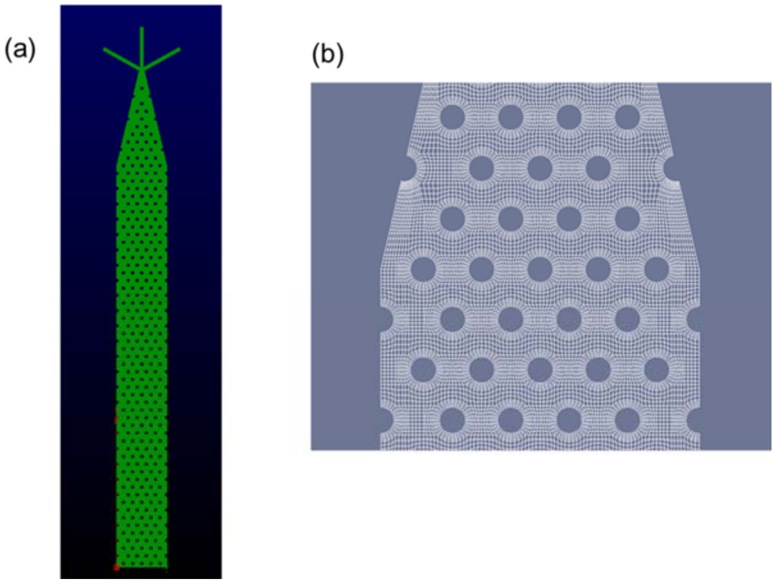

Figure S3 (a) An overview of the computational domain representing the interior space of the post microreactor (b) Details of the mesh employed in the simulation

A no-slip boundary condition and zero contact angle were specified at the channel and post walls. At the channel inlets, the flow rates of the two phases were specified, and a zero-gradient condition was set for the pressure. At the channel outlet, a zero-gradient boundary condition for velocity and phase fraction was applied, and the pressure was set to be the atmospheric value.

S2. Flow regime and comparison

S2.1 Gas-liquid flow regime

We compared our experimentally obtained flow regime maps with similar systems reported in the literature. Wada *et al.* reported oxygen and ethyl acetate gas/liquid flow regimes in the same post reactor configuration within similar superficial velocity ranges, we therefore compared our nitrogen/ethanol gas/liquid flow regime map with the one obtained by Wada *et al.* [7]. Figure S4 shows that despite the difference in the type of gas and liquid employed, we were still able to observe highly similar flow regimes and transition boundaries.

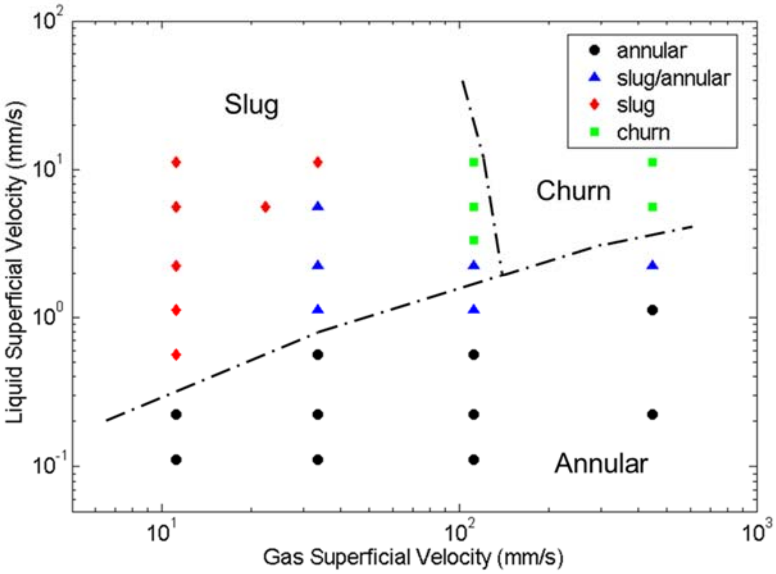

Figure S4 Comparison of nitrogen/ethanol gas/liquid flow regime map with the flow regime transition boundaries for oxygen/ethyl acetate flows using the post microreactor as reported by Wada *et al.* [7]. The data points represent nitrogen/ethanol flow regimes produced in the current work. The dash-dot lines represent the transition boundaries in oxygen/ethyl acetate biphasic flows reported by Wada *et al.*.

For other types of pillared channels, Krishnamurthy *et al.* studied the flow of nitrogen/water across an array of staggered circular micropillars (100 μm in height and 100 μm in diameter). [8, 9] Moreover, De Loos *et al.* reported nitrogen/water flow through rectangular micro channels containing round pillars (50 μm in height and 30 μm in diameter). [10] For both studies, the gas and liquid flow rate ranges were several orders of magnitude higher than the ranges in our work (in both cases, the liquid superficial velocities ranged above 10 mm/s, and gas superficial velocities were above 100 mm/s), which makes it difficult for direct comparison. The difference in operating ranges is due to the fact that the post microreactor in our work is intended for performing multiphase reactions, which requires a certain amount of residence time for the reaction to complete. For example, for a typical condition for the oxidation reaction of amines, the liquid superficial velocity was 0.62 mm/s, and the gas superficial velocity was 70 mm/s, which corresponded to a residence time of ~1 s. Higher flow rates would lead to shorter residence times, and may compromise the conversion of reaction. Therefore, the flow regime maps in our work have focused on a liquid superficial velocity range of $10^{-1} – 10^{2}$ mm/s, and a gas superficial velocity range of $10^{1} – 10^{3}$ mm/s.

An interesting phenomenon in the work by Krishnamurthy *et al.* was the bridged flow regime, which refers to a region between the slug flow regime and the annular flow regime where the gas slugs merged and the liquid phase spanned the channel in the form of bridges between the posts. [8]

In our system, we were able to occasionally observe a single liquid bridge between the two posts in the slug/annular flow regime, but the bridge occurred only very infrequently, and is not a distinct hydrodynamic feature of the slug/annular flow regime (Figure S5). The difference may be attributed to the difference in flow rates and geometry. First, in the study of Krishnamurthy *et al.*, the system was operating under superficial velocities that were several orders of magnitude higher than our system. The rapid flow and strong shear have prevented the liquid bridges from coalescing due to interfacial tension. Second, the pillar arrays studied by Krishnamurthy *et al.* had a height of 100 μm, whereas the posts in our system had a height of 300 μm. The shallower inter-post space in the system of Krishnamurthy *et al.* means that it is more likely for the liquid phase to be trapped between two posts, and less likely for the liquid bridges to be deconstructed by coalescence.

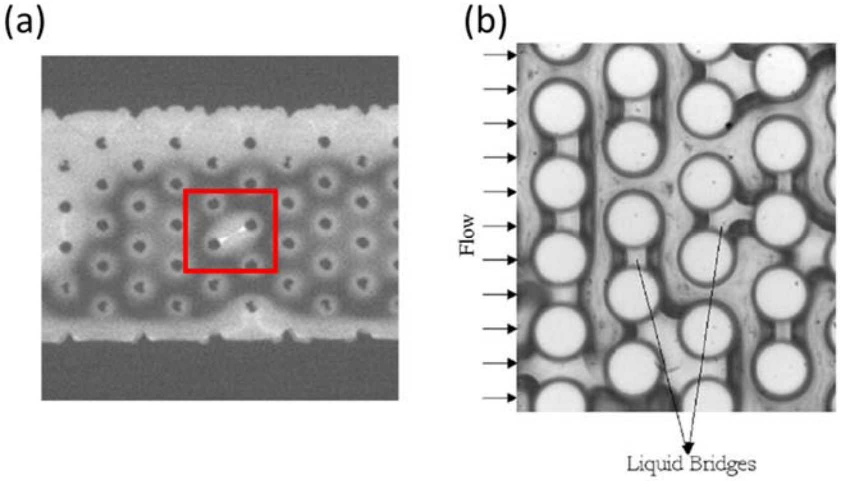

Figure S5. (a) A liquid bridge observed in the slug/annular flow regime in the post microreactor (b) Liquid bridges observed in the pillared channel studied by Krishnamurthy *et al.* [8] Reproduced with permission from Elsevier, 2009.

Additionally, we compared our gas/liquid flow regime map with the flow regimes in the microscale and milliscale packed-bed reactors. Two typical gas/liquid flow regimes exist in the packed-bed reactor, namely, the trickling regime (where a continuous gas phase flows through the interstices, and the surface of the packing is covered by trickling streams or films of the liquid phase), and the pulsing regime (where gas-rich and liquid-rich zones pass through the reactor in an alternating manner). [11] Charpentier *et al.* studied the trickling to pulsing regime transition boundary in a milliscale packed-bed reactor with a packing size of ~3 mm. [12] Losey *et al.* fabricated a microscale packed-bed reactor containing ~50 μm particles as packing, and reported the transition boundary between the trickling and pulsing regimes. [11] Here, we plotted the transition boundaries reported by Charpentier *et al.* and Losey *et al.* on top of the gas/liquid flow regime map in the post microreactor (Figure S6). It was to be expected that the location of the transition boundary was sensitive to the size of the packing particle, as demonstrated by the difference between the results of Charpentier *et al.* and Losey *et al.*. More notably, the trickling to pulsing regime transition boundary in the microscale packed-bed reactor with ~50 μm particles (the dot-dash line) was found to be in good agreement with the annular to slug regime transition boundary in the post microreactor with 50 μm posts.

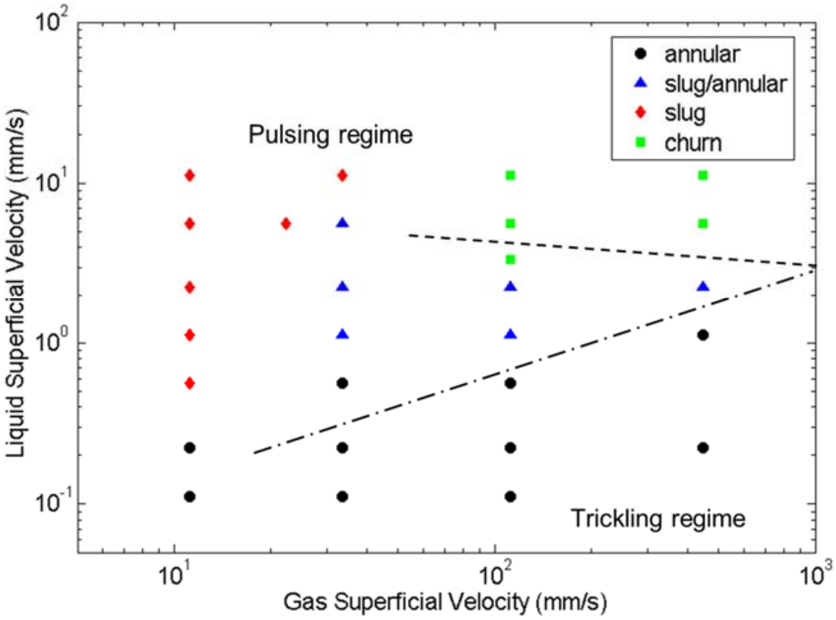

Figure S6. Comparison of the gas/liquid flow regime map in the post microreactor with the trickling to pulsing flow regime transition boundaries studied on the microscale (dot-dash line) [11] and on the milliscale (dotted line) [12].

S2.2 Liquid-liquid flow regime

Compared to gas-liquid flow, there are fewer literature reports discussing liquid-liquid flow regime transitions in microscale multiphase flow systems. Zhao *et al.* studied the flow patterns of immiscible liquids (water and kerosene) in a 300 μm wide and 600 μm deep microchannel. [13] They examined a wide range of biphasic flow rates, and plotted the flow regime map in terms of the *Weber* numbers, *We*, for water and kerosene (Figure S7b).

To compare with their findings, we also plotted the ethanol-fluorinert flow regime map in the post microreactor using *We*, shown in Figure S7. For ease of direct comparison, we plotted the non-wetting phase on the vertical axis and the wetting phase on the horizontal axis. Within the same range of Weber numbers ($We_{wetting} = 10^{-7}{\sim}10^{-2}, We_{non-wetting} = 10^{-6}{\sim}10^{-1}$), in the flow regime map by Zhao *et al.*, there is an almost horizontal transition boundary between the slug flow regime and the parallel flow regime at $We_{non-wetting} = 10^{-4}{\sim}10^{-3}$. Similarly, in our system, we observed a horizontal transition boundary from the slug flow regime to the annular flow regime, also at $We_{non-wetting} = 10^{-4}{\sim}10^{-3}$. In both cases, the flow regime transition was primarily driven by an increase in the flow rate of the non-wetting phase.

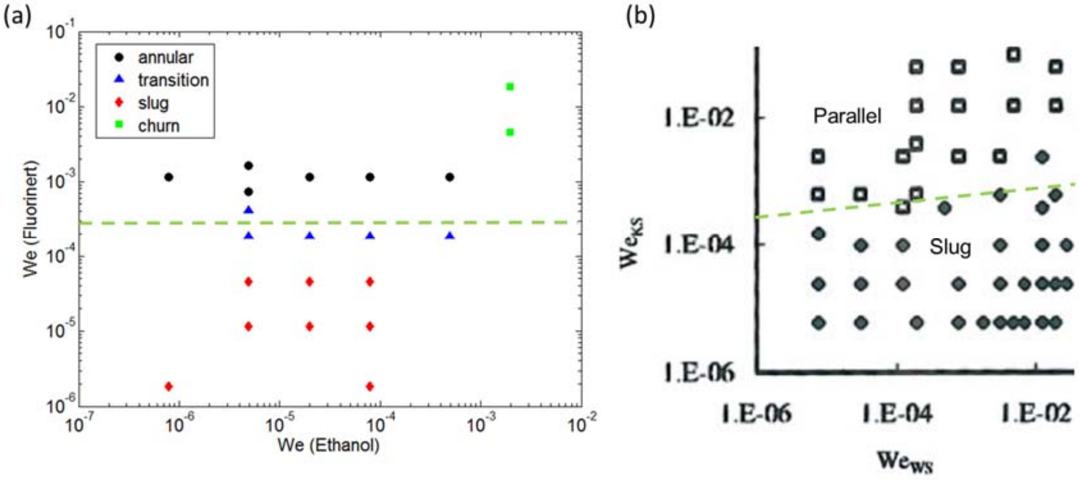

Figure S7. (a) The liquid/liquid flow regime map in the post microreactor (b) The liquid/liquid flow regime map in a rectangular microchannel as reported by Zhao *et al.* [13] The flow regime maps are both plotted in Weber numbers for ease for comparison. The green dashed lines represent the boundary of flow regime transition. Reproduced with permission from Wiley-VCH, 2006.

S2.3 Flow regime maps in dimensionless numbers

We have primarily examined the flow regime and transitions in terms of superficial velocities following conventions in the field. [7-10, 14] In addition, there are several dimensionless numbers that are important for characterizing microscale multiphase flow: *Reynolds*, *Re*, *capillary*, *Ca*, and *We* number. We have therefore plotted the flow regime maps in terms of *Re*, *Ca* and *We*, shown in Figures S8-10.

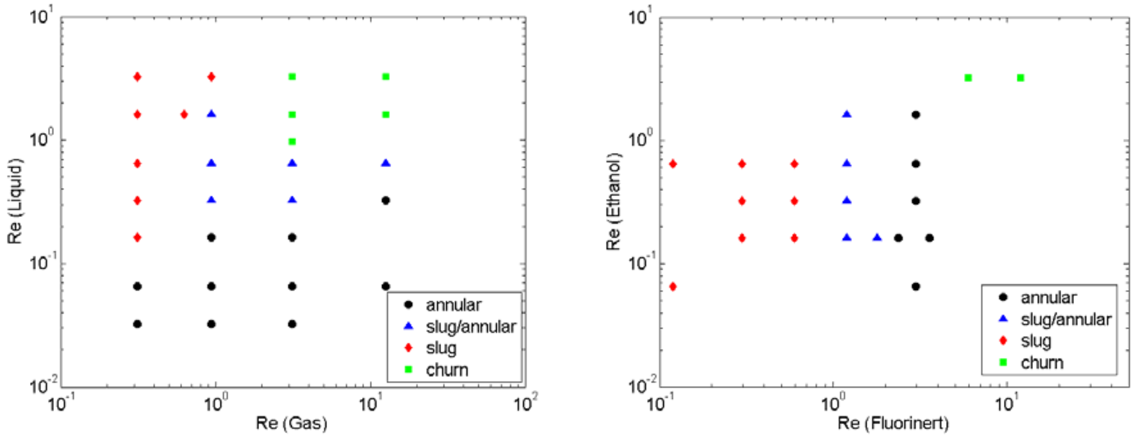

Figure S8. Flow regime maps in terms of biphasic Reynolds numbers

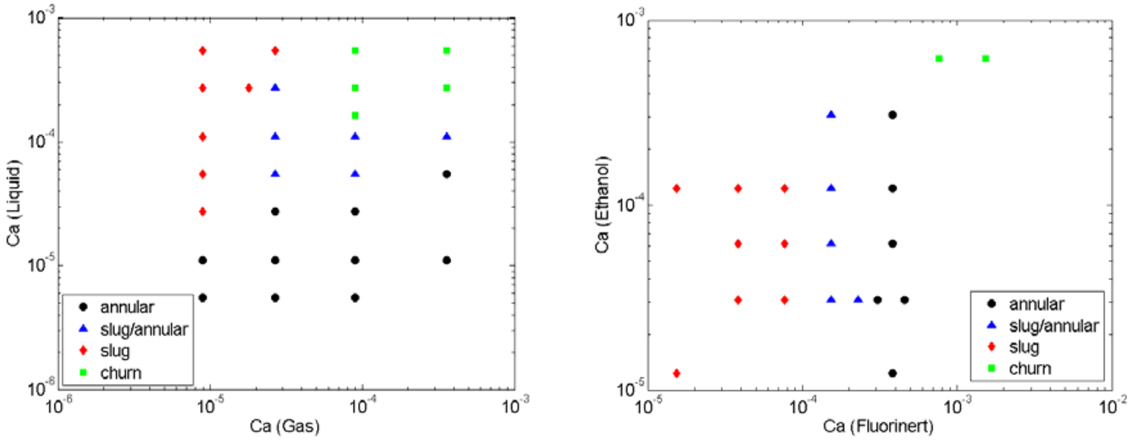

Figure S9. Flow regime maps in terms of biphasic capillary numbers

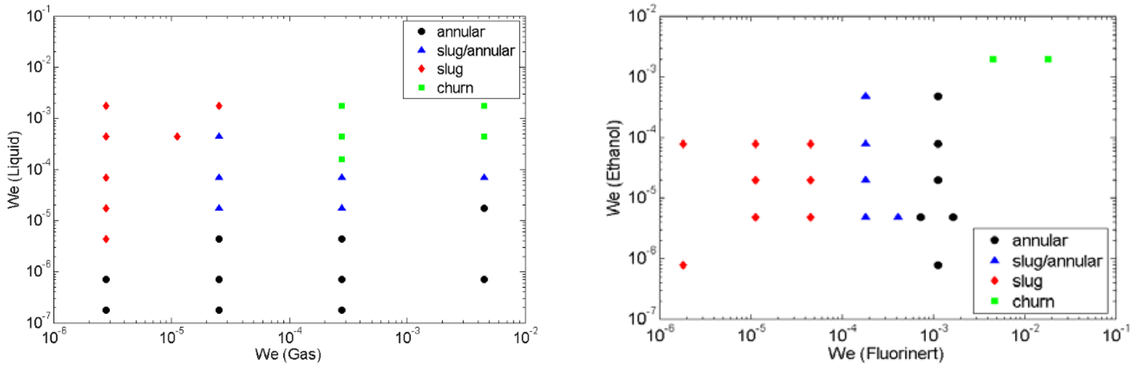

Figure S10. Flow regime maps in terms of biphasic Weber numbers

S3. Mass transfer analysis

S3.1 Justification of the application of the penetration theory:

Before calculating the mass transfer coefficient in the post microreactor using the penetration theory, it is important to justify its applicability. Based on the derivation of the Penetration theory, [15] there are two key assumptions: (1) The liquid film is thick; (2) Diffusion is dominant in the direction normal to the interface.

Here we examine the applicability of the above-mentioned assumptions to the post microreactor studied here. For the contour interface between the bulk of two phases, the posts essentially serve as static mixers that enhance the mixing within each phase, so that each phase can be considered to be homogeneous in concentration. Therefore, the concentration gradient which drives mass transfer is confined to a region near the phase interface. As the biphasic flow at the interface is primarily parallel to the phase boundary, diffusion is the dominant form of mass transfer in the direction normal to the interface. Therefore, the application of the penetration theory is justified.

For the mass transfer process taking place on the post wetting layers, although the non-wetting phase can be regarded as homogenously well-mixed, the wetting film tends to become quickly saturated over time due to its limited thickness, resulting in a smaller concentration difference and a weaker driving force for interfacial mass transfer. Therefore, for the post wetting layer, the penetration theory provides an upper bound for the mass transfer coefficient. With this overestimation, we calculated that the mass transfer coefficient at the posts is one or two orders of magnitude smaller than that at the contour. Therefore, overall, it is acceptable to apply the penetration theory to estimate the overall mass transfer coefficients with reasonable accuracy.

Moreover, to decipher the mass transfer contributions of the contour interface and the post wetting layers, Equation 8 in the paper uses a simple additive rule to sum up the k_La values from the two parts. In reality, since the post wetting layer tends to get saturated over time, the driving force for mass transfer at the posts will eventually be smaller than that at the contour. By using a simple additive rule, we overestimated the mass transfer contribution from the posts. However, as we have pointed out, even with this overestimation, the k_La contribution of the post wetting layers is still one to two orders of magnitude smaller than that of the contour. Therefore, this approximation does not introduce significant deviation in the final results.

S3.2 Justification of the choice of the characteristic length scale:

The inter-post distance was chosen as the characteristic length scale for the following scenarios in the post microreactor: (1) The slug contour in the slug/annular flow, (2) the annular flow and (3) the churn flow. The choice was made since the contour is composed of segments of interface pinned between pairs of posts, and each segment can be regarded as a relatively isolated unit for interfacial mass transfer. The choice has also been validated by an experimentally measured k_La value (Figure S11).

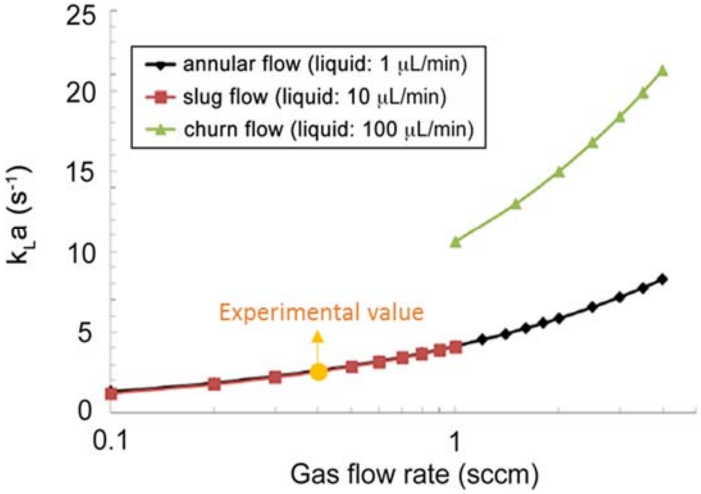

Figure S11. Comparison between the predicted mass transfer coefficients and the published experimental value by Wada *et al.* [7].

S3.3 Justification of the surface regeneration rate:

The penetration theory applied in our analysis (Equation 1) assumes that the interface is regenerated after each time interval t_c. Here, we examine the validity of this assumption. For the contour interface, according to the definition (Equation 2), the contact time refers to the time scale during which the two phases "slip" past each other a distance that equals the characteristic length, or the inter-post distance in this case. This indicates that after the contact time, the interface will be completely regenerated due to the slip.

For the post wetting layer, the contact time $t_{c,p}$ is defined as the "life time" of the post wetting layer, which is the time during which the posts are surrounded by the slug formed by the non-wetting phase, and mass transfer takes place. After the slug passes, the posts will be again submerged in the wetting phase, and the wetting layer will be regenerated at this time until the non-wetting slug encounters the posts again. This regeneration time scale for the post wetting layer is $t_{r,p}$. Therefore, the question boils down to whether it is possible to regenerate the wetting film on the posts within $t_{r,p}$, when the posts are submerged in the wetting phase. The ratio of $t_{c,p}$ and $t_{r,p}$ can be approximated as the ratio of the non-wetting phase holdup, $\varepsilon_{non-wetting}$, and the wetting phase holdup, $\varepsilon_{wetting}$. Because $\varepsilon_{non-wetting} < \varepsilon_{wetting}$ in the slug flow regime, so $t_{c,p} < t_{r,p}$. When considering the diffusive contribution to mass transfer alone, we showed in Figure 5c of the manuscript that $t_{c,p} > \tau_D$ (τ_D is the diffusive time scale estimated from the film thickness). Therefore, $t_{r,p} > \tau_D$, meaning that for the post wetting film, the regeneration period is longer than the diffusive time scale. Moreover, in addition to diffusion, convection would also contribute to further enhancing the rate of mass transfer during regeneration. Therefore, the regeneration time, $t_{r,p}$, is sufficiently long to renew the liquid film on the posts.

It is also important to note that based on our calculation, the $k_{\mathrm{L}}a$ contribution of the contour interface is one to two orders of magnitude higher than that of the post wetting layer, so the $k_{\mathrm{L}}a$ of the contour interface determines the accuracy of the calculation.

S3.4 Three-Dimensional structure of the post wetting layer:

The wetting film thickness captured in the visualization experiment ($\sim 30\ \mu m$) appears thicker than the wetting film in a typical slug flow system (several microns). The discrepancy may stem from the existence of the wetting meniscus between the posts and the walls. As shown in the side view of a wetted post (Figure S12c), the wetting phase forms menisci at the top and bottom corners of the posts. Since the LIF technique visualizes the fluorescence emitted from the wetting phase, the measured post wetting layer thickness ($L_{measure} \approx 30\ \mu m$) will appear larger than the wetting film thickness on the posts (usually few microns thick). In the manuscript, we used $L_{measure}$ to estimate the diffusive time scale τ_D ($\tau_D \approx 0.9$s), which is in fact an upper bound of the actual diffusive time scale, and this upper bound is still lower than the life time of the wetting layer (shown in Figure 5c of the manuscript). Therefore, we arrive at the same conclusion that, between regenerations, the wetting film has become almost fully saturated by solute transported from the non-wetting phase.

The same point is also illustrated by the comparison between simulation and experiment: The wetting layer is captured by numerical simulations, but the layer appears thinner than the "halos" around the posts as shown in the microscopic images (Figure S12a-b). This is again because the "halos" from the LIF visualization include all the fluorescence emitted from the wetting phase surrounding the posts, and is approximately the $L_{measure}$ in Figure S12c. On the other hand, the numerical simulations were two-dimensional for the purpose of saving computation time, which essentially sampled a reactor cross-section as shown in Figure S12c. Therefore, the wetting film in the simulations would appear thinner that what was captured experimentally.

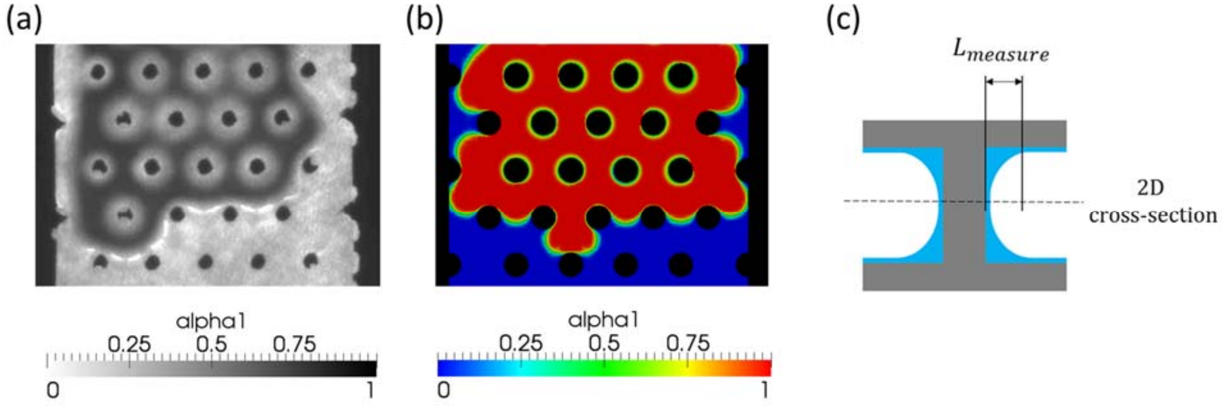

Figure S12. (a) The post wetting layer captured by the LIF visualization (b) and the VOF simulation. (c) Scheme of the side view of a post with wetting layer

S3.5 Comparison of mass transfer coefficients with literature:

Having obtained the mass transfer coefficients from the penetration theory calculations, we compared our results with previously published work in similar systems. Wada *et al.* reported the experimentally obtained mass transfer coefficients in a post microreactor.[7] The measured mass transfer coefficient compares well with our prediction from the penetration theory (Figure S11). For the mass transfer coefficients in other related microreactor systems, Losey *et al.* reported that the overall mass transfer coefficients in packed-bed microreactors with particle sizes of 50 – 75 µm ranged from 5 to 15 s^{-1}. [11] Kashid *et al.* have comprehensively reviewed the mass transfer performance for gas/liquid and liquid/liquid flows in microchannels. [16] For gas/liquid flows, the mass transfer coefficient normally ranges from 0.1 – 20 s^{-1}, while for liquid/liquid flows, the mass transfer coefficient tends to be on the order of 0.01 – 1 s^{-1}. In general, the orders of magnitude of the reported k_La values agrees with our calculation from the penetration theory.

References

1. C. A. Schneider, W. S. Rasband and K. W. Eliceiri, *Nat Methods*, 2012, 9, 671-675.
2. J. Schindelin, I. Arganda-Carreras, E. Frise, V. Kaynig, M. Longair, T. Pietzsch, S. Preibisch, C. Rueden, S. Saalfeld, B. Schmid, J. Y. Tinevez, D. J. White, V. Hartenstein, K. Eliceiri, P. Tomancak and A. Cardona, *Nat Methods*, 2012, 9, 676-682.
3. C. W. Hirt and B. D. Nichols, *J Comput Phys*, 1981, 39, 201-225.
4. E. Berberovic, N. P. van Hinsberg, S. Jakirlic, I. V. Roisman and C. Tropea, *Phys Rev E*, 2009, 79.
5. J. U. Brackbill, D. B. Kothe and C. Zemach, *J Comput Phys*, 1992, 100, 335-354.
6. H. G. Weller, G. Tabor, H. Jasak and C. Fureby, *Comput Phys*, 1998, 12, 620-631.

7. Y. Wada, M. A. Schmidt and K. F. Jensen, *Ind Eng Chem Res*, 2006, 45, 8036-8042.
8. S. Krishnamurthy and Y. Peles, *Phys Fluids*, 2007, 19.
9. S. Krishnamurthy and Y. Peles, *Int J Multiphas Flow*, 2009, 35, 55-65.
10. S. R. A. de Loos, J. van der Schaaf, R. M. Tiggelaar, T. A. Nijhuis, M. H. J. M. de Croon and J. C. Schouten, *Microfluid Nanofluid*, 2010, 9, 131-144.
11. M. W. Losey, M. A. Schmidt and K. F. Jensen, *Ind Eng Chem Res*, 2001, 40, 2555-2562.
12. J. C. Charpentier and M. Favier, *Aiche J*, 1975, 21, 1213-1218.
13. Y. C. Zhao, G. W. Chen and Q. Yuan, *Aiche J*, 2006, 52, 4052-4060.
14. K. A. Triplett, S. M. Ghiaasiaan, S. I. Abdel-Khalik and D. L. Sadowski, *Int J Multiphas Flow*, 1999, 25, 377-394.
15. E. L. Cussler, *Diffusion: Mass Transfer in Fluid Systems*, Cambridge University Press, Cambridge Cambridgeshire ; New York, 2009.
16. M. N. Kashid, A. Renken and L. Kiwi-Minsker, *Chem Eng Sci*, 2011, 66, 3876-3897.